Hindawi
Journal of Renewable Energy
Volume 2018, Article ID 7898679, 18 pages
https://doi.org/10.1155/2018/7898679

Research Article

Model-Based Control Design of Series Resonant Converter Based on the Discrete Time Domain Modelling Approach for DC Wind Turbine

Yu-Hsing Chen, Catalin Gabriel Dincan, Philip Kjær, Claus Leth Bak, Xiongfei Wang, Carlos Enrique Imbaquingo, Eduard Sarrà, Nicola Isernia, and Alberto Tonellotto

Department of Energy Technology, Aalborg University, Aalborg, Denmark

Correspondence should be addressed to Catalin Gabriel Dincan; cgd@et.aau.dk

Received 24 August 2018; Accepted 31 October 2018; Published 2 December 2018

Academic Editor: Shuhui Li

This paper focuses on the modelling of the series resonant converter proposed as a DC/DC converter for DC wind turbines. The closed-loop control design based on the discrete time domain modelling technique for the converter (named SRC#) operated in continuous-conduction mode (CCM) is investigated. To facilitate dynamic analysis and design of control structure, the design process includes derivation of linearized state-space equations, design of closed-loop control structure, and design of gain scheduling controller. The analytical results of system are verified in z-domain by comparison of circuit simulator response (in PLECS™) to changes in pulse frequency and disturbances in input and output voltages and show a good agreement. Furthermore, the test results also give enough supporting arguments to proposed control design.

1. Introduction

MEDIUM-voltage DC (MVDC) collection of wind power is an attractive candidate to reduce overall losses and installation cost, especially within offshore HVDC-connected wind generation as illustrated in Figure 1 [1]. To connect DC wind turbine with MVDC network ($\pm 50\text{kV}_{\text{DC}}$), the series resonant converter (SRC) serves as a step-up solid-state transformer as shown in Figure 2. With the series resonant converter, the DC turbine converter can take advantages of high efficiency, high voltage transformation ratio, and galvanic fault isolation for different ratings of turbine generator [2–6].

Traditional closed-loop control of SRC for the DC distribution system is easily implemented by detecting the zero-crossing of the resonant inductor current i_r and controlling the length of transistor and diode conduction angle α without considering circuit parameters of SRC [7]. Additionally, the output power flow control of SRC for DC network is achieved by controlling the phase-shift angle and frequency between the two arms of H-bridge inverter [6, 8, 9].

Based on the discrete time domain modelling approach, the small-signal model of an improved SRC (named SRC#) is proposed [9, 10]. This paper continues with the small-signal plant model addressed in Section 3 and the Appendix and mainly focuses on the closed-loop control design for the system. In the following sections, the mode of operation of SRC# and small-signal plant model based on the discrete time domain modelling approach will be briefly introduced first. The structure of closed-loop control based on the proposed small-signal plant model and the improvement in the disturbance rejection capability will be revealed. To satisfy the power flow control with variable switching frequency, the gain scheduling technique will be given. Finally, the analytical solution of overall system is revealed and verified by comparing with time-domain trace in circuit simulation model implemented in PLECS™ under different operating points. Furthermore, the proposed control deign will be demonstrated by a scaled-down laboratory test bench.

2. Mode of Operation of Series Resonant Converter

The mode of operation of series resonant converter (SRC#) in Figure 2 is decided by the ratio between natural frequency

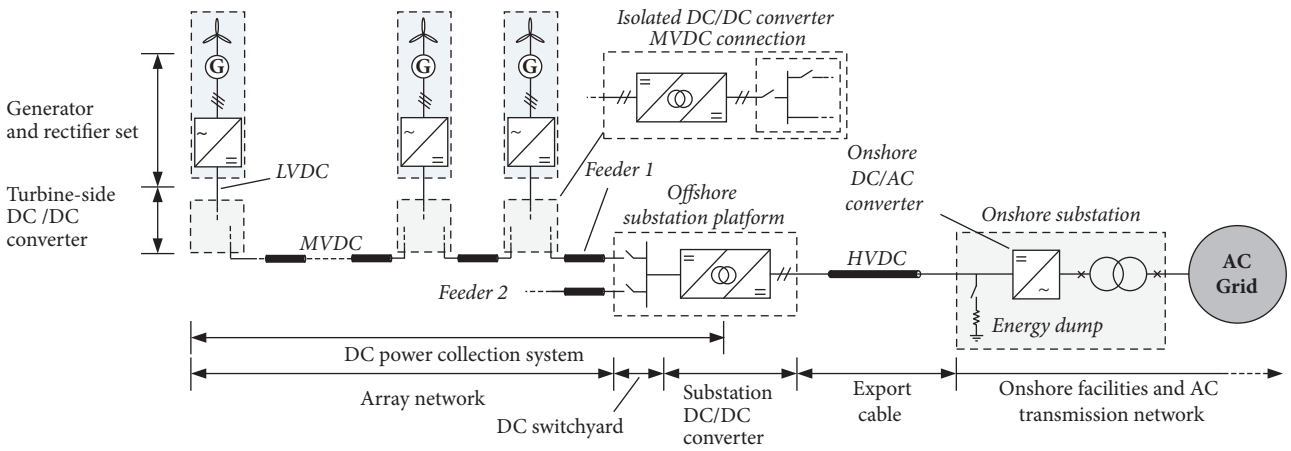

Figure 1: Generic configuration of the wind power plant with MVDC power collection.

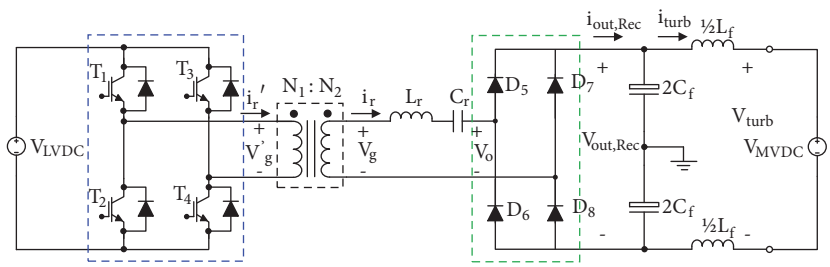

Figure 2: Circuit topology of series resonant converter (SRC#).

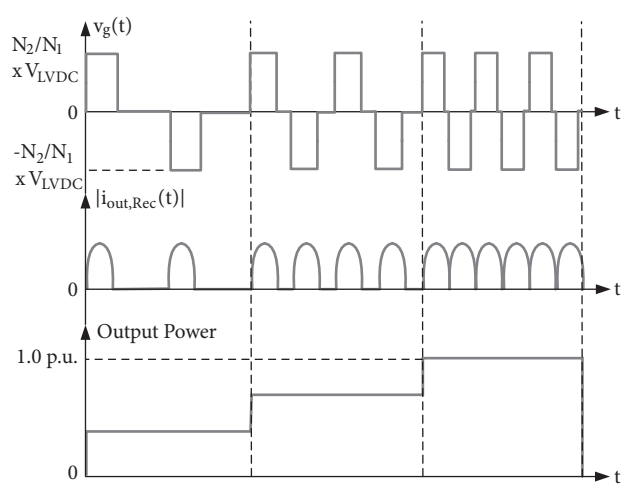

Figure 3: Frequency-depended power flow control of SRC#.

of tank (L_r and C_r) and the switching frequency of H-bridge inverter: subresonant, resonant, and super resonant mode. In subresonant mode, the switching frequency of H-bridge inverter is lower than the natural frequency of tank. The resonant operating mode is selected when the switching frequency is equal to the natural frequency of tank. If converter's switching frequency is higher than the natural frequency of tank, the converter is operated in the super resonant mode [9].

Contrasting with the constant frequency with phase shift control which is normally applied for operation in super resonant mode, to achieve ZVS at turn-on, Figure 3 illustrates the concept of frequency-depended power flow control of SRC#. The converter leg of SRC# consisting of switches T_1 and T_2 is referred to as the leading leg and the one consisting of switches T_3 and T_4 is referred to as the lagging leg as indicated in Figure 2. Both converter legs operate at a 50% duty cycle [6, 9].

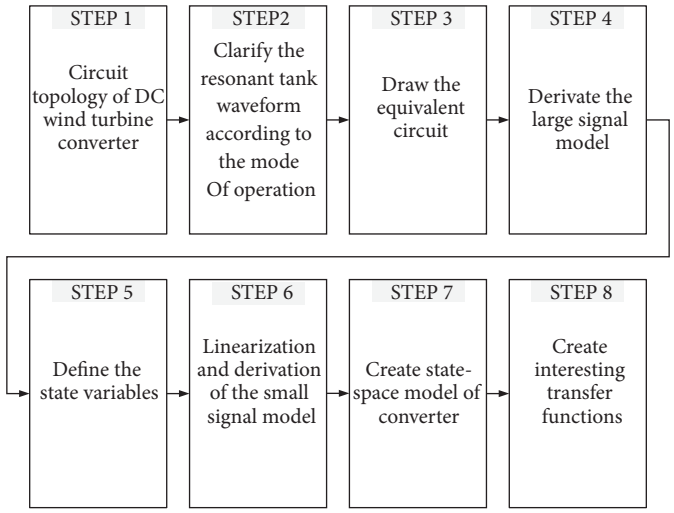

Figure 4: Flow chart of derivation of plant model of SRC#.

To achieve ZCS character at turn-off or minimize the turn-off current, the IGBT-based SRC# is designed to operate at subresonant continuous-conduction mode (subresonant CCM). This control design can drive the implemented phase shift having the same length as the resonant pulse without sacrificing the advantage of linear relation to the number of resonant pulses, as depicted in Figure 3. Compared to a traditional SRC with frequency control design in subresonant mode, therefore, the medium frequency transformer in the SRC# addressed in this paper can be designed for a higher frequency and avoids saturation for lower frequencies.

3. Discrete Time Domain Modelling Approach for Series Resonant Converter

Considering the efficiency, subresonant mode is selected for the mode of operation of SRC# for the DC wind turbine [5, 6]. Based on the circuit topology shown in Figure 2, Figure 5 illustrates the steady-state voltage and current waveforms of SRC# in subresonant mode, where ω_s is the switching frequency ($\omega_s = 2\pi \cdot f_s$) of SRC#. To apply the linear control theory to the SRC# control design, deriving the plant model of SRC# with the discrete time domain modelling approach includes the derivation of large-signal equations based on the interesting interval shown in Figure 5, linearization of discrete state equations, and derivation of small-signal transfer function. In the derivation, the voltages $v_{MVDC}(t)$ and $v_{LVDC}(t)$ are assumed to be discrete in nature, having the constant values $V_{o(k)}$ and $V_{g(k)}$ in interval of k_{th} event, and then switch to next states $V_{o(k+1)}$ and $V_{g(k+1)}$ at the start of $(k+1)_{th}$ event. This procedure is only valid when the variation in $v_o(t)$ or $v_g(t)$ in the event is relatively smaller than its initial and final values [10].

With the discrete time domain modelling approach, (1) gives a linearized state-space model of SRC# in subresonant mode and the transfer functions between input state variables and the defined interesting states are shown in (3) and (5). To simplify the derivation, the output filter of SRC# (i.e., L_f and C_f) is neglected and only the DC component of output current diode rectifier $i_{out,Rec}$ is selected as an output variable I_o.

To obtain the harmonic model of DC turbine converter, Figure 4 gives a complete flow chart of mathematical derivation of SRC# plant model, which describes how the SRC# plant model is obtained. First of all, the circuit topology and mode of operation are decided as shown in Figures 2 and 5 and then the equivalent circuit based on the switching sequence of transistors is generated in Figure 6. Based on the circuit topology shown in Figure 2, Figure 5 illustrates the voltage and current waveforms of SRC# n subresonant mode and the equivalent circuit for each event (switching interval) is given in Figure 6. According to Figure 6, the large signal model of converter is created (step 4) and then the interesting state variables (step 5) are defined to generate the small-signal equation and the space model of converter as in steps 6 and 7, respectively ([A], [B], [C], and [D]). Eventually, the converter plant model (power stage of converter) is established based on the interesting transfer function (g_1, g_2, and g_3, in step 8). The correction of model (plant model) has been confirmed and the details of derivation are given in the Appendix.

$$\begin{bmatrix} \dot{\tilde{x}}_1 \\ \dot{\tilde{x}}_2 \end{bmatrix} = [A] \begin{bmatrix} \tilde{x}_1 \\ \tilde{x}_2 \end{bmatrix} + [B] \begin{bmatrix} \tilde{\alpha} \\ \tilde{V}_g \\ \tilde{V}_o \end{bmatrix}$$
$$\tilde{I}_o = [C] \begin{bmatrix} \tilde{x}_1 \\ \tilde{x}_2 \end{bmatrix} + [D] \begin{bmatrix} \tilde{\alpha} \\ \tilde{V}_g \\ \tilde{V}_o \end{bmatrix} \quad (1)$$

where

$$\tilde{x}_1 = \tilde{I}_r,$$
$$\tilde{x}_2 = \tilde{v}_{cr} \quad (2)$$

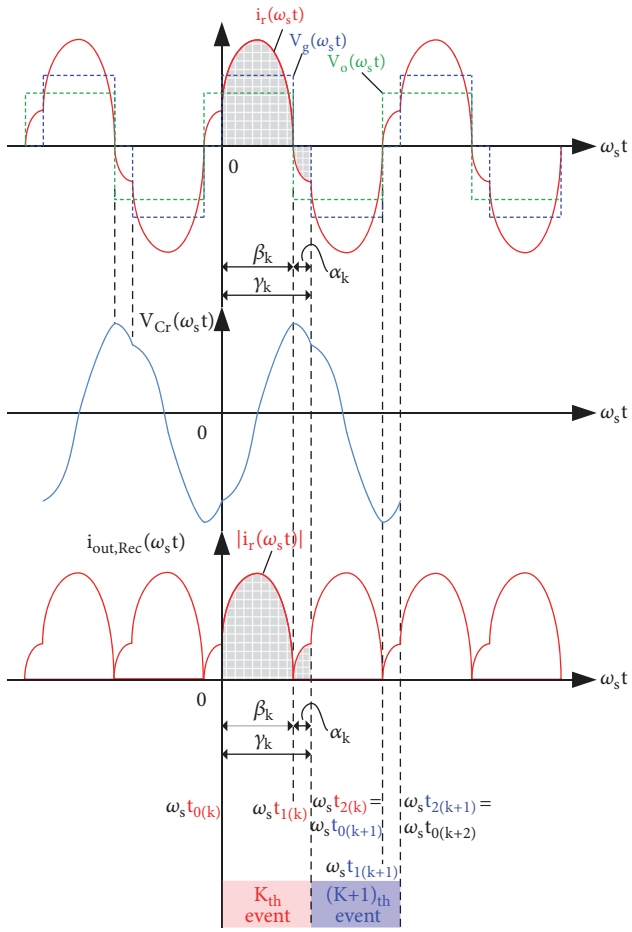

Figure 5: Resonant inductor current and resonant capacitor voltage waveforms of SRC# in subresonant CCM.

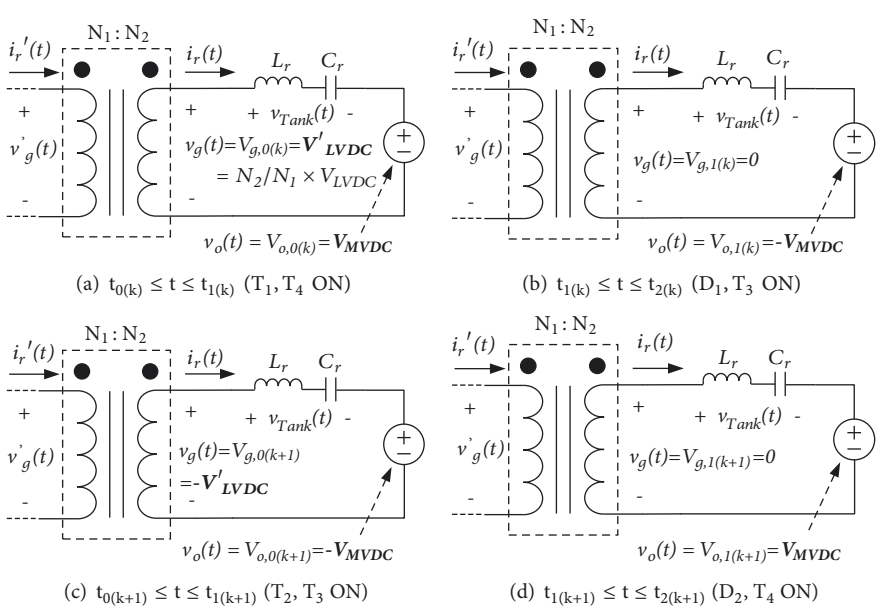

Figure 6: Equivalent circuit of SRC for large-signal analysis of conduction intervals in subresonant CCM.

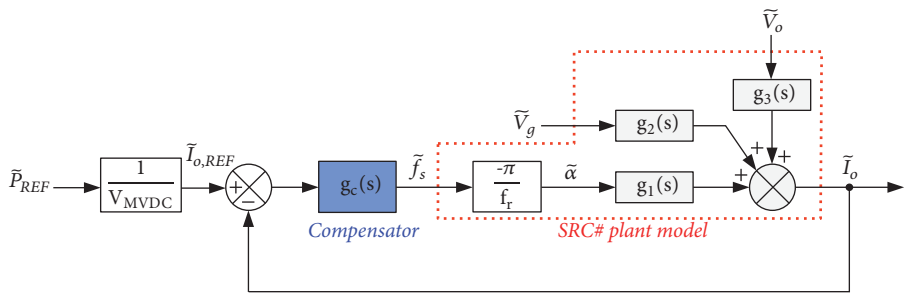

Figure 7: Small-signal control model of the series resonant converter SRC# in subresonant CCM.

and the derivation of $[A]$, $[B]$, $[C]$, and $[D]$ matrixes is shown in the Appendix. Transfer functions between defined internal state variables and input states are given by

$$\widetilde{X} = \begin{bmatrix} \widetilde{I}_r \\ \widetilde{v}_{cr} \end{bmatrix} = \begin{bmatrix} \widetilde{x}_1 \\ \widetilde{x}_2 \end{bmatrix} = \begin{bmatrix} g_{xu,11} & g_{xu,12} & g_{xu,13} \\ g_{xu,21} & g_{xu,22} & g_{xu,23} \end{bmatrix} \begin{bmatrix} \widetilde{\alpha} \\ \widetilde{V}_g \\ \widetilde{V}_o \end{bmatrix} \quad (3)$$

where

$$\begin{aligned} g_{xu,11} &= \left.\frac{\widetilde{I}_r}{\widetilde{\alpha}}\right|_{\widetilde{V}_g(s)=0,\widetilde{V}_0(s)=0}, \\ g_{xu,12} &= \left.\frac{\widetilde{I}_r}{\widetilde{V}_g}\right|_{\widetilde{\alpha}(s)=0,\widetilde{V}_0(s)=0}, \\ g_{xu,13} &= \left.\frac{\widetilde{I}_r}{\widetilde{V}_o}\right|_{\widetilde{\alpha}(s)=0,\widetilde{V}_g(s)=0} \\ g_{xu,21} &= \left.\frac{\widetilde{v}_{cr}}{\widetilde{\alpha}}\right|_{\widetilde{V}_g(s)=0,\widetilde{V}_0(s)=0}, \\ g_{xu,22} &= \left.\frac{\widetilde{v}_{cr}}{\widetilde{V}_g}\right|_{\widetilde{\alpha}(s)=0,\widetilde{V}_0(s)=0}, \\ g_{xu,23} &= \left.\frac{\widetilde{v}_{cr}}{\widetilde{V}_o}\right|_{\widetilde{\alpha}(s)=0,\widetilde{V}_g(s)=0} \end{aligned} \quad (4)$$

and transfer functions between converter output current and input state variables are

$$\widetilde{I}_o(s) = \left[g_1(s) \quad g_2(s) \quad g_3(s)\right] \begin{bmatrix} \widetilde{\alpha} \\ \widetilde{V}_g \\ \widetilde{V}_o \end{bmatrix} \quad (5)$$

where the transfer functions $g_1(s)$, $g_2(s)$, and $g_3(s)$ can be obtained via

$$\left[g_1(s) \quad g_2(s) \quad g_3(s)\right] = C(SI - A)^{-1} B + D, \quad (6)$$

$$\begin{aligned} g_1(s) &= \left.\frac{\widetilde{I}_o(s)}{\widetilde{\alpha}(s)}\right|_{\widetilde{V}_g(s)=0,\widetilde{V}_0(s)=0}, \\ g_2(s) &= \left.\frac{\widetilde{I}_o(s)}{\widetilde{V}_g(s)}\right|_{\widetilde{\alpha}(s)=0,\widetilde{V}_0(s)=0}, \\ g_3(s) &= \left.\frac{\widetilde{I}_o(s)}{\widetilde{V}_0(s)}\right|_{\widetilde{\alpha}(s)=0,\widetilde{V}_g(s)=0} \end{aligned} \quad (7)$$

The transfer function $g_1(s)$ describes how the output current $\widetilde{I}_o$ is influenced by the control input variable $\widetilde{\alpha}$ and the transfer functions $g_2(s)$ and $g_3(s)$ describe how the output current $\widetilde{I}_o$ is affected if any disturbance occurs in input voltage V_g ($\propto$ V_{LVDC}) and the output voltage V_o ($\propto$ V_{MVDC}). For example, the array network (MVDC grid) contains voltage harmonics. The transfer function $g_3(s)$ can be used to evaluate the effect of voltage harmonics on the converter output current. Detailed derivation of the above linearized state-space model and the expression of elements in [A], [B], [C], and [D] matrix in (1) have been revealed in the Appendix.

4. Model-Based Closed-Loop Control Design

Figure 7 gives an overview of small-signal control model of SRC# based on the average plant model in (5) and (6). The control design of SRC# includes derivation of small-signal plant model and the design of the compensator g_c. The small-signal transfer functions of SRC# between converter output current and input state variables are given by (5) and (6), where the output current variation is the expression of linear combination of the three independence inputs. The relationship between α and f_s in subresonant CCM in large-signal model is

$$\alpha = \left(\frac{1}{2f_s} - \frac{1}{2f_r}\right) 2\pi f_s = \pi - \frac{\pi}{f_r} f_s \quad (8)$$

where

$$f_r = \frac{1}{2\pi\sqrt{L_r C_r}} \quad (9)$$

By substituting the perturbation terms of small-signal analysis into expression in (8), the small-signal expression of α and f_s can be obtained

$$\overline{\alpha} + \widetilde{\alpha} = \pi - \frac{\pi}{f_r}\left(\overline{f_s} + \widetilde{f}_s\right) \quad (10)$$

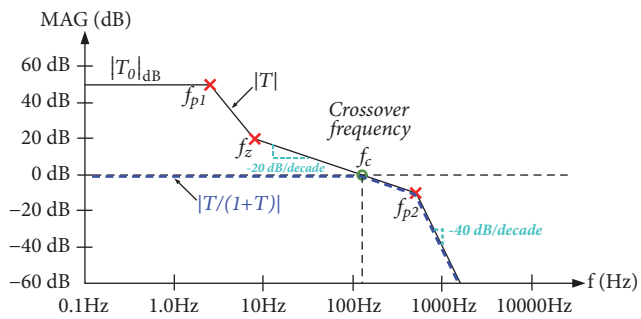

Figure 8: Illustration of magnitude asymptote of desired loop gain $T(s)|_{\text{target}}$ (target curve of loop gain) [11].

where the AC component is

$$\tilde{\alpha} = -\frac{\pi}{f_r}\tilde{f}_s \tag{11}$$

Eventually, the system transfer function in Figure 5 can be expressed as

$$\begin{aligned}\tilde{I}_o(s) = {} & \frac{(1/V_{MVDC})\, g_c(-\pi/f_r)\, g_1}{1 + g_c(-\pi/f_r)\, g_1}\tilde{P}_{REF} \\ & + \frac{g_2}{1 + g_c(-\pi/f_r)\, g_1}\tilde{V}_g \\ & + \frac{g_3}{1 + g_c(-\pi/f_r)\, g_1}\tilde{V}_o\end{aligned} \tag{12}$$

Equation (12) can be further expressed as the following:

$$\tilde{I}_o(s) = \frac{1}{V_{MVDC}}\frac{T}{1+T}\tilde{P}_{REF} + \frac{g_2}{1+T}\tilde{V}_g + \frac{g_3}{1+T}\tilde{V}_o \tag{13}$$

with a *loop gain*.

$$T(s) = g_c\frac{-\pi}{f_r}g_1 \tag{14}$$

where the *loop gain* is defined by the product of gains around forward and feedback paths [11].

5. Disturbance Rejection Capability

The closed-loop control design of SRC# is implemented via the compensator g_c, which is applied to shape the loop gain of the system (i.e., $T(s)$). Considering the transfer function of output current given in (13), the relationship between $\tilde{I}_o$ and $\tilde{V}_g$ is shaped by closed-loop control as

$$\left.\frac{\tilde{I}_o(s)}{\tilde{V}_g(s)}\right|_{\tilde{P}_{REF}=0,\tilde{V}_0=0} = \frac{g_2}{1+T} \tag{15}$$

The variation in output current I_o caused by $\tilde{V}_g$ can be alleviated by increasing the magnitude of the loop gain $T(s)$ when the closed-loop control design is integrated with the SRC# plant model. The system transfer functions in (13) also show that the variation reduction of I_o due to variation in MVDC network will benefit from a high loop gain $T(s)$:

$$\left.\frac{\tilde{I}_o(s)}{\tilde{V}_0(s)}\right|_{\tilde{P}_{REF}=0,\tilde{V}_g=0} = \frac{g_3}{1+T} \tag{16}$$

Furthermore, consider the tracking performance of output current control in (17).

$$\left.\frac{\tilde{I}_o(s)}{\tilde{P}_{REF}}\right|_{\tilde{V}_g=0,\tilde{V}_o=0} = \frac{1}{V_{MVDC}}\frac{T}{1+T} \tag{17}$$

Assume that a constant power reference P_{REF} is applied to the control loop with a constant MVDC source and a constant LVDC source. A large loop gain $|T(s)|$ (i.e., $|T(s)| \gg 1$) can also make sure of a good DC current tracking performance as shown in (18)

$$\frac{\bar{I}_o}{\bar{P}_{REF}} \approx \frac{1}{V_{MVDC}} \tag{18}$$

Therefore, the objective of the compensator g_c is to govern the system with a desired loop gain (i.e., $T(s) = T(s)|_{\text{target}}$), where the deviation of desired loop transfer function $T(s)|_{\text{target}}$ can be found by simply evaluating the magnitude asymptote in Figure 8:

$$\begin{aligned}T(s) &= g_c\frac{-\pi}{f_r}g_1 \\ &= T_0 \times \frac{(1 + s/\omega_z)}{\left(1 + s/Q\omega_{p1} + \left(s/Q\omega_{p1}\right)^2\right)\left(1 + s/\omega_{p2}\right)}\end{aligned} \tag{19}$$

Considering the desired loop gain $T(s)|_{\text{target}}$ illustrated in Figure 8, the disturbance rejection capability of the output current for a frequency range below the crossover frequency (f_c) can be improved with closed-loop control. For example, at the low frequency range ($f < f_c$), the output current I_o is almost in direct proportion to the power reference signal P_{REF}.

$$\begin{aligned}&\frac{T}{1+T} \approx \begin{cases} 1 & \text{for } f < f_c \ (|T| \gg 1) \\ T & \text{for } f > f_c \ (|T| \ll 1)\end{cases} \Longrightarrow \\ &\left.\frac{\tilde{I}_o(s)}{\tilde{P}_{REF}}\right|_{\tilde{V}_g=0,\tilde{V}_o=0} \approx \frac{1}{V_{MVDC}}\end{aligned} \tag{20}$$

Furthermore, a high loop gain provides a good disturbance reduction to the variation on input voltage V_g and output voltage V_o by the factor $1/|T|$.

$$\frac{1}{1+T} \approx \begin{cases} \frac{1}{T} & for\ f < f_c\ \ (|T| \gg 1) \\ 1 & for\ f > f_c\ \ (|T| \ll 1) \end{cases} \Longrightarrow$$

$$\left.\frac{\widetilde{I}_o(s)}{\widetilde{V}_g(s)}\right|_{\widetilde{P}_{REF}=0,\widetilde{V}_0=0} \approx \frac{g_2}{T}, \qquad \left.\frac{\widetilde{I}_o(s)}{\widetilde{V}_0(s)}\right|_{\widetilde{P}_{REF}=0,\widetilde{V}_g=0} \approx \frac{g_3}{T} \tag{21}$$

Typically, the *crossover frequency* f_c should be less than approximately 10% of switching frequency of SRC# ($f_c < 0.1 f_s$) to limit the harmonics caused by PWM switching [11]. Based on (19), therefore, compensator $g_c|_{OP}$ under a certain operating point (OP) can be expressed by

$$g_c|_{OP} = \frac{T|_{OP,\text{target}}}{(-\pi/f_r)\, g_1|_{OP}} = \frac{f_r}{-\pi} \cdot \frac{1}{g_1|_{OP}} \left.\frac{T_0 \times (1+s/\omega_z)}{\left(1+s/Q\omega_{p1}+\left(s/Q\omega_{p1}\right)^2\right)\left(1+s/\omega_{p2}\right)}\right|_{OP,\text{target}} \tag{22}$$

Equations (23)–(27) summarize the parameters (i.e., Q, ω_{p1}, ω_{p2}, ω_z, ω_c, and θ) which are used to shape the loop gain $T(s)$ via the compensator g_c. The crossover frequency f_c and the low-frequency pole at f_{p1} are defined as

$$f_c = 0.1 f_s, \tag{23}$$

$$f_{p1} = \frac{1}{4.5} f_c \tag{24}$$

The low-frequency zero at f_z and high-frequency pole at f_{p2} can be chosen according to crossover frequency f_c and required phase margin θ as follows:

$$f_z = f_c \sqrt{\frac{1-\sin(\theta)}{1+\sin(\theta)}}, \tag{25}$$

$$f_{p2} = f_c \sqrt{\frac{1+\sin(\theta)}{1-\sin(\theta)}} \tag{26}$$

where the angle θ is a phase lead angle of compensator at f_c. The DC gain of target loop gain $T(s)|_{\text{target}}$ is

$$T_o = \left(\frac{f_c}{f_{p1}}\right)^2 \times \sqrt{\frac{f_z}{f_{p2}}} \tag{27}$$

The *Q-factor* is used to characterize the transient response of closed-loop system. Using a high *Q-factor* can increase the dynamic response during transient, but it can also cause overshoot and ringing on power devices. In practical application, the *Q-factor* must be sufficiently low to keep enough phase margins and alleviate voltage and current stress on power devices [11]. Additionally, since the power flow control of SRC# depends on the control of switching frequency f_s, the parameters of target curve and the coefficient of transfer function g_c have to be changed according to different operating points (different output powers). To make sure that the compensator g_c can match with different output power requirements, therefore, a gain scheduling approach is proposed which will be revealed in the next section.

Table 1: Parameters of SRC# plant model.

Low voltage DC (V_{LVDC})	4.04 (kV_{DC})
Medium voltage DC (V_{MVDC})	100.0 (kV_{DC})
Transformer winding voltage ratio (N_1: N_2)	1: 25
Rated output power P_{out}	10 (MW)
Resonant inductor L_r	78.1 (mH)
Resonant capacitor C_r	0.25 (uF)

6. Design of Digital Gain Scheduling Controller

Gain scheduling controller is designed to access the parameter of compensator g_c in real time and then adjust it based on the different operating points. Figure 9 gives a complete digital controller of SRC# based on the small-signal control model and the bilinear transformation. The digital controller of SRC# consists of a small-signal controller, a gain scheduling controller, a feedforward control loop, and a DC component calculator (I_o calculator). The controller is implemented in z-domain with a variable interrupt frequency f_{int} ($f_{int} \propto$ switching frequency f_s). With the bilinear transform, the general form of the discrete-time representation of the compensator g_c can be expressed as

$$g_c(z) = \frac{a_5 z^5 + a_4 z^4 + a_3 z^3 + a_2 z^2 + a_1 z + a_0}{b_5 z^5 + b_4 z^4 + b_3 z^3 + b_2 z^2 + b_1 z + b_0} \tag{28}$$

where coefficients a_n and b_n (n=0~5) are used to specify the coefficients of numerator and denominator.

To design the gain scheduling controller, coefficients a_n and b_n in (28) are evaluated under different operating points (i.e., different output power) with (22)–(27). A trend in the variation of each coefficient (i.e., P_{REF} vs. a_n and b_n) is recorded and then is formulated via the polynomial approximation as shown in Figures 12 and 13 which will be discussed in the next section (Section 7). Eventually, the coefficient of $g_c(z)$ for SRC# in the subresonant CCM can be adjusted by a continuous function such as $a_n = f(P_{REF})$ and $b_n = f(P_{REF})$ in real time to avoid any potential turbulences caused by gain-changing.

7. Verification of Closed-Loop Control Design

With the SRC# topology in Figure 2 and the controller shown in Figure 9, Tables 1 and 2 give the parameters used in the state-space model and circuit simulation models (tools)

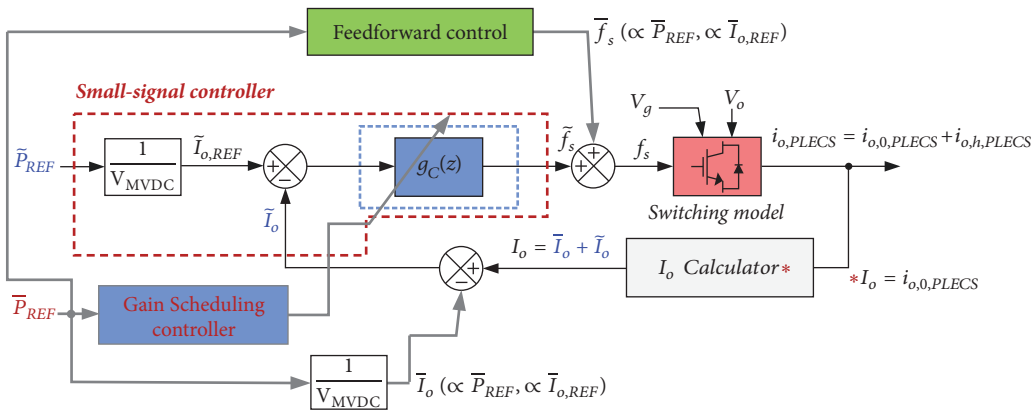

Figure 9: Control block of the series resonant converter SRC# in z-domain.

Table 2: Specifications of digital controller.

Switching frequency f_s	1.0k (Hz) (full load)
Interrupt frequency of digital controller f_{int} (i.e. $f_{int} = 2f_s$)	2.0k (Hz) (full load)
Q-factor	1.0
Phase margin θ	52°
Power reference signal P_{REF}	10MW (full load)
Sampling rate of A/D conversion	1M (Hz)
Duty cycle	50%

Table 3: Specifications of laboratory test bench.

Low voltage DC source (V_{LVDC})	216 (V_{DC})
DC component of medium voltage source ($V_{MVDC,0}$)	400 (V_{DC})
Transformer winding voltage ratio (N_1: N_2)	1: 2
Rated output power P_{out}	550 (W)
Resonant inductor L_r	20.0 (mH)
Resonant capacitor C_r	1.0 (uF)
Switching frequency f_s	800 (Hz)
Output filter inductor L_f	2.5 (mH)
Output filter capacitor C_f	1.0 (mF)
Resistive load R_{load}	125 (Ω)
Interrupt frequency f_{int} (i.e. $f_{int} = 2f_s$)	1.6k (Hz)
Sampling rate of A/D conversion	1M (Hz)
Duty cycle	50%

for verifying the validation of overall system in z-domain. The control model in the subresonant CCM is verified to identify the accuracy of proposed small-signal model, and then the results of coefficient assessment of $g_c(z)$ with the gain scheduling controller are integrated with control loop and are tested by a ramp-power reference.

By applying a +0.5% stepping perturbation to all input state variables, Figures 10 and 11 give the analytical solutions of small-signal model of SRC# and the results obtained from the time-domain switching model implemented in PLECS™. The SRC# with closed-loop control is commanded to deliver around 9.0MW DC power and 7.5MW DC power to MVDC network, respectively. Figures 10 and 11 show that both the steady state and transient state in the analytical model match with the results generated by switching model. Therefore, dynamics of SRC# switching model can be predictable and controlled with the proposed small-signal model.

Figures 12 and 13 give the result of coefficient assessment of $g_c(z)$ for the design of the gain scheduling controller. Based on (28), the trend in the variation of coefficients a_n and b_n in subresonant CCM from 5.75MW to 10MW (0.5MW/step) is identified and then the variation of each coefficient is approximated with a 3rd polynomial (i.e., $a_n(P_{REF})|_{PolyFit}$ and $b_n(P_{REF})|_{PolyFit}$). According to the variation in output power reference P_{REF}, the gain scheduling controller accesses the polynomial $g_c(z)$ to regulate its coefficient in real time. To evaluate the adequacy of control design of overall system, finally, the time-trace simulation of output power flow control is given in Figure 14 with a ramp-power reference P_{REF} from 0.1MW to 10MW, and vice versa. The results show that the output current/power (I_o) of the series resonant converter can be well controlled when magnitude output powers references are changed.

8. Laboratory Test Results

To verify the control design, first the circuit simulation is carried out with circuit simulation tool of PLECS™, and then the controller is implemented in a scaled-down laboratory test bench. The circuit configuration of test bench and the corresponding parameters are shown in Figure 15 and Table 3, respectively, where the MVDC network is simulated

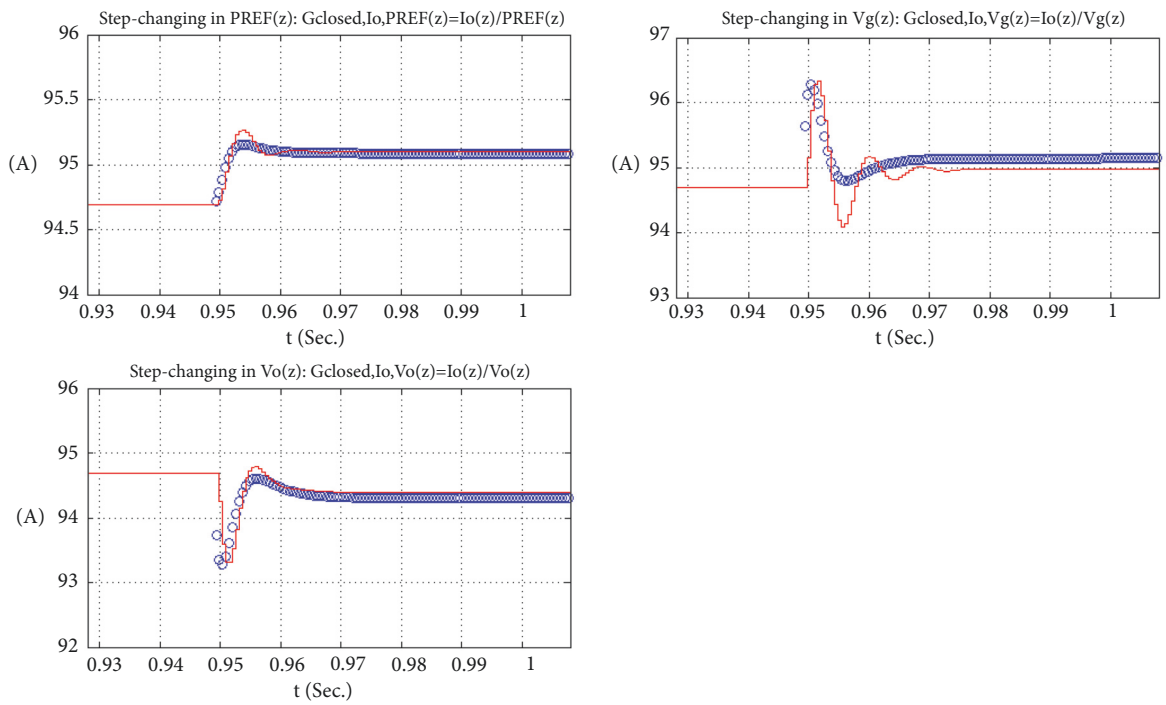

FIGURE 10: Dynamics of output current I_o generated by both the switching model and derived state-space model with the closed-loop controller when +0.5% of step-changing is applied in P_{REF}, V_g, and V_o, respectively (P_{REF}: 9.0MW $\longrightarrow$ 9.045MW, V_g: 101.01kV$_{DC}$ $\longrightarrow$ 101.515kV$_{DC}$, V_o: 100.0kV$_{DC}$ $\longrightarrow$ 100.5kV$_{DC}$; blue circle: dynamic of state-space model in z-domain, red line: dynamic of electrical signal in *PLECS* circuit model, the interrupt time of digital controller: T_{int}=1/(2x$f_s|_{op}$) =1/(2x900Hz) sec).

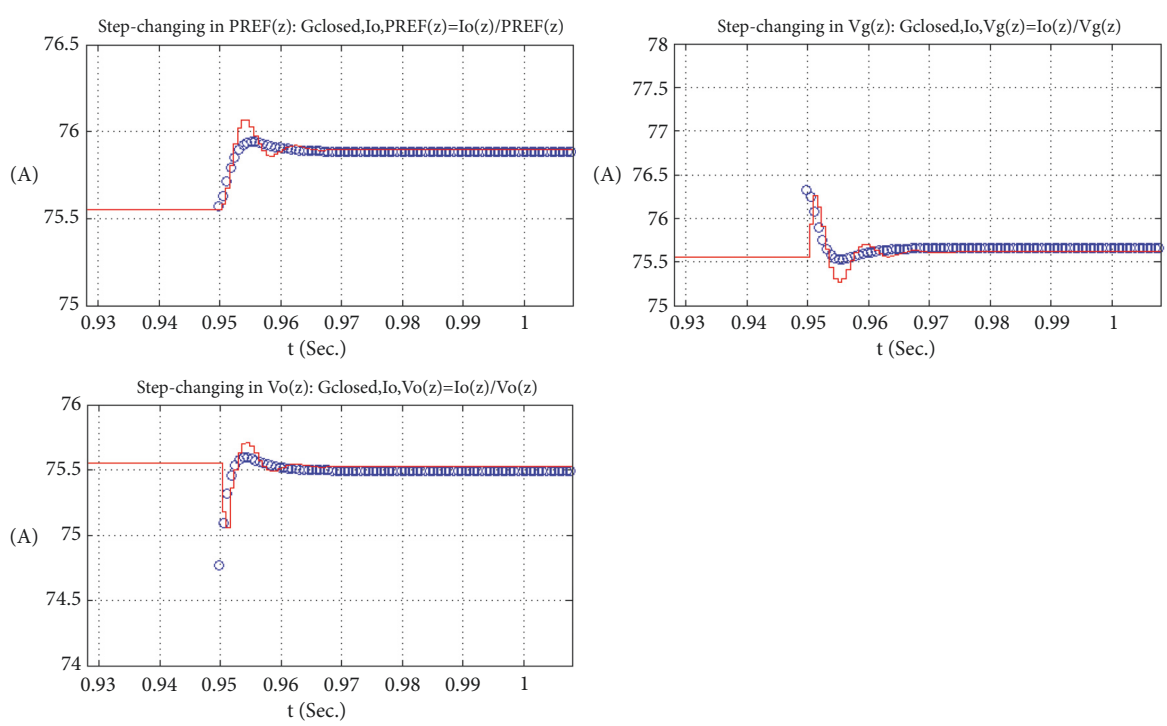

FIGURE 11: Dynamics of output current I_o generated by both the switching model and derived state-space model with the closed-loop controller when +0.5% of step-changing is applied in P_{REF}, V_g, and V_o, respectively (P_{REF}: 7.5MW $\longrightarrow$ 7.5375MW, V_g: 101.01kV$_{DC}$ $\longrightarrow$ 101.515kV$_{DC}$, V_o: 100.0kV$_{DC}$ $\longrightarrow$ 100.5kV$_{DC}$; blue circle: dynamic of state-space model in z-domain, red line: dynamic of electrical signal in *PLECS* circuit model, the interrupt time of digital controller: T_{int}=1/(2x$f_s|_{op}$) =1/(2x750Hz) sec).

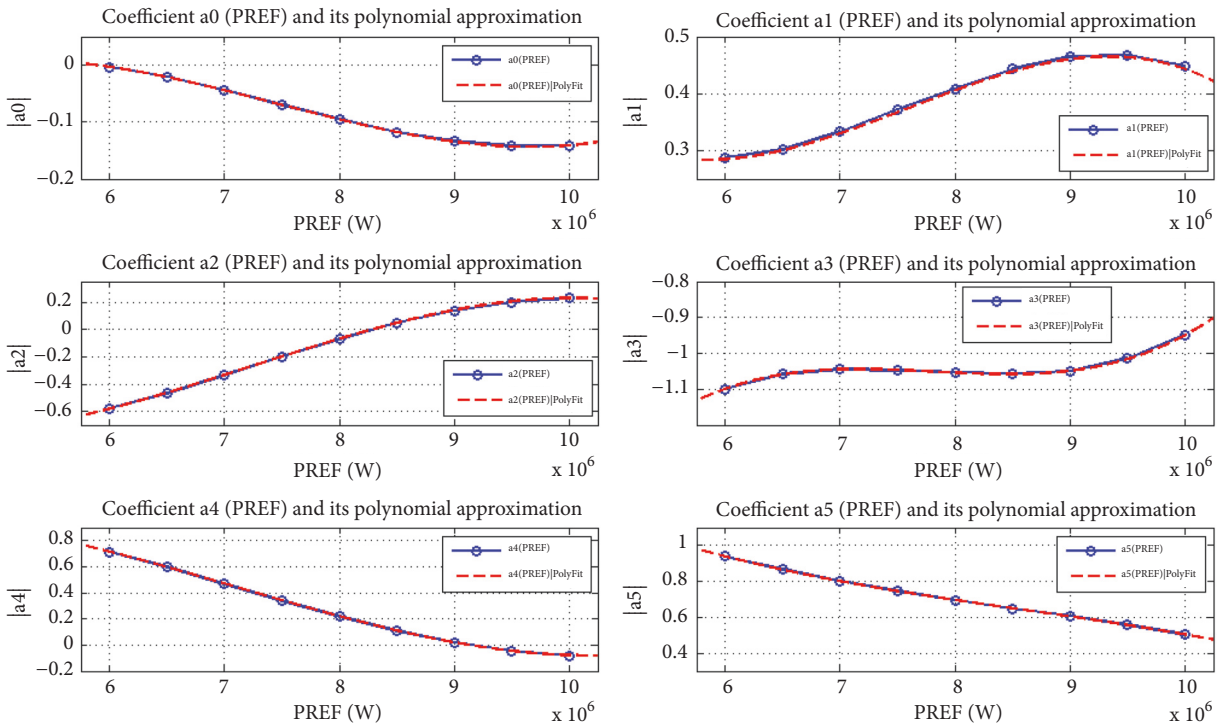

FIGURE 12: Design of gain scheduling controller: piecewise continuous functions of numerator of $g_c(z)$ and its polynomial approximation (3rd) in subresonant CCM.

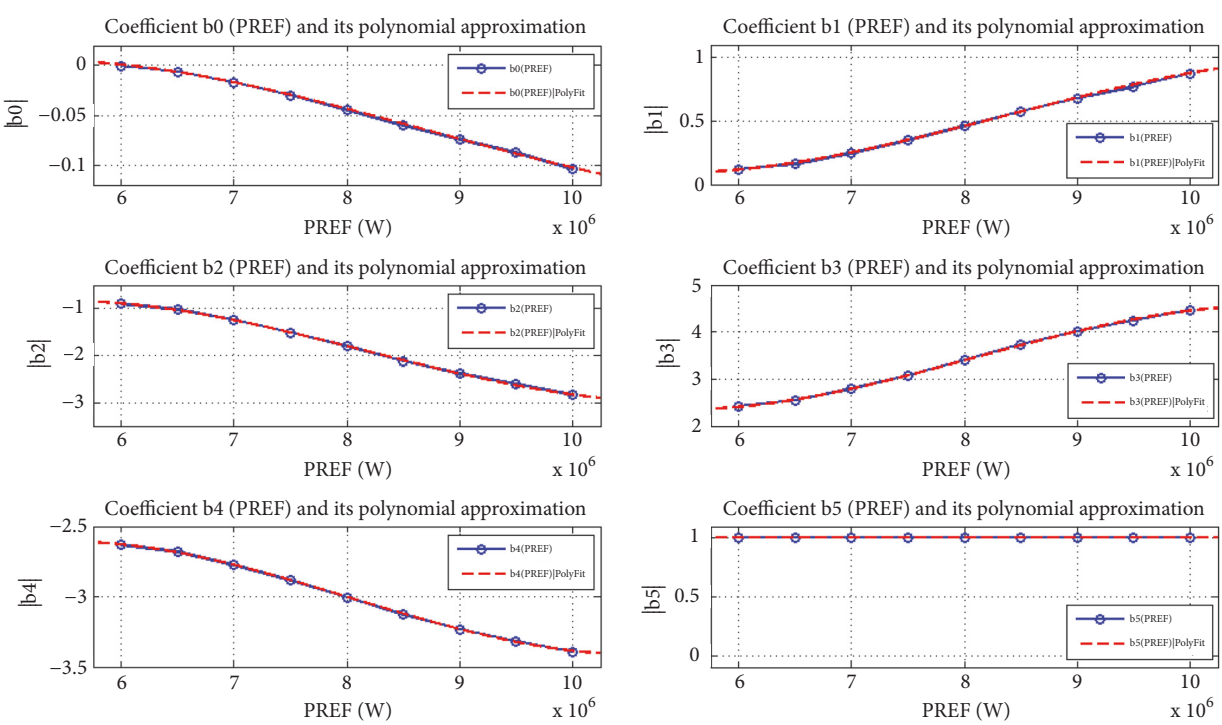

FIGURE 13: Design of gain scheduling controller: piecewise continuous functions of denominator of $g_c(z)$ and its polynomial approximation (3rd) in subresonant CCM.

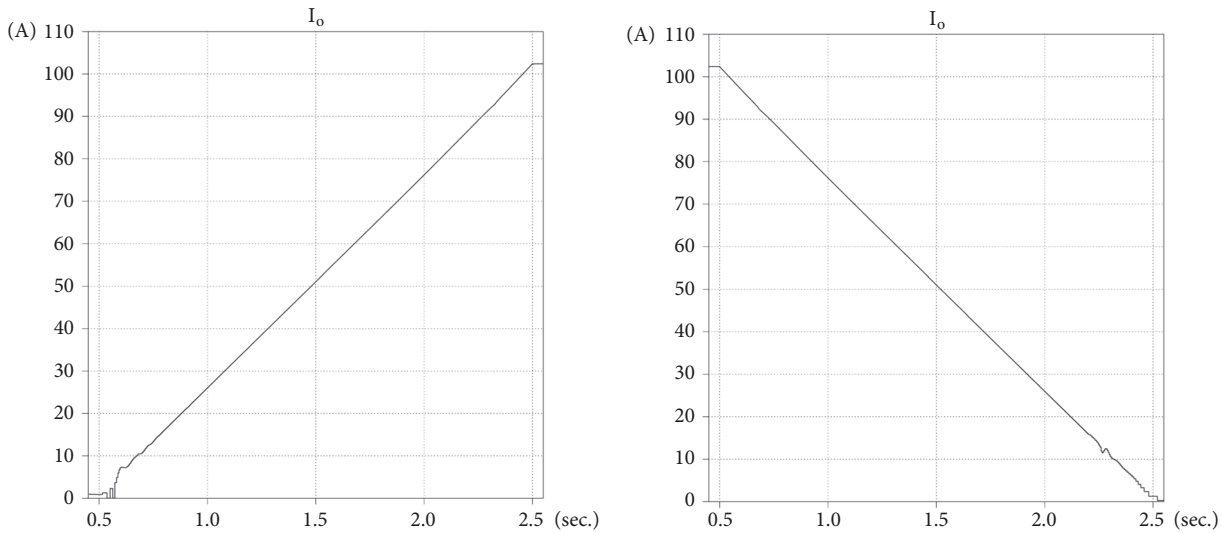

(a) Ramp-up power: $P_{REF}=P_{out}=0.1MW \longrightarrow 10MW$, slop=4.95MW/sec

(b) Ramp-down power: $P_{REF}=P_{out}=10MW \longrightarrow 0.1MW$, slop=-4.95MW/sec

Figure 14: Output current (I_o) of the series resonant converter with a ramp-power reference P_{REF} to verify the design of gain scheduling controller and demonstrate the start-up process of DC wind converter.

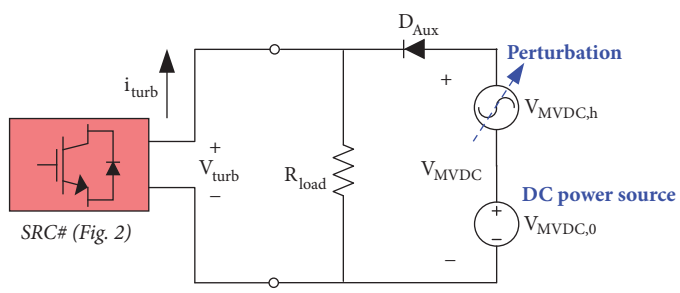

Figure 15: Configuration of laboratory test bench ($V_{MVDC,0}$: DC component of medium voltage power source, $V_{MVDC,h}$: perturbation source).

by a unidirectional power flow DC power source with a controllable perturbation.

Figures 16(a) and 16(b) depict the system response when a positive and a negative step perturbation (0.01p.u) in MVDC network are applied, respectively. The control design exhibits a close behavior in either simulation or experimental test. There is some small tracking error during the transient between the simulation and test results. This usually is caused by the estimated error of components and stray inductance which is not considered in simulation model. Figure 16(c) represents how the output current behaves when a step-change (0.26p.u) is applied in the power reference signal P_{REF}. Under the proposed control law for SRC#, both the simulation and test result show that the DC component of DC turbine output current ($\bar{i}_{turb}$) tracking performance can be guaranteed. However, a small oscillation ($\approx 40Hz$) during the transient of step-change of power reference signal in the experimental test is observed due to the series diode D_{Aux} (in Figure 15) which is reverse-biased at this test occasion.

9. Conclusion

A model-based control design of SRC# for DC wind power plant based on small-signal plant model in the discrete time-domain modelling is revealed. This paper continues with the modelling of SRC# given in the Appendix and mainly addresses the closed-loop control design for the system. The control design process contains the derivation of state-space plant model, design of closed-loop control structure, and design of gain scheduling controller. Compared with the traditional frequency-depended power flow control which relied on open-loop structure, the SRC# with the closed-loop structure can gain a better disturbance rejection capability for the output power control. The verification of proposed digital controller including plant model is addressed in both the analytical model and the time-domain circuit simulation implemented in PLECS™ in Section 7 by evaluating the SRC# with the stepping-perturbation under the subresonant CCM. Furthermore, gain scheduling approach is implemented by the polynomial approximation and tested under different

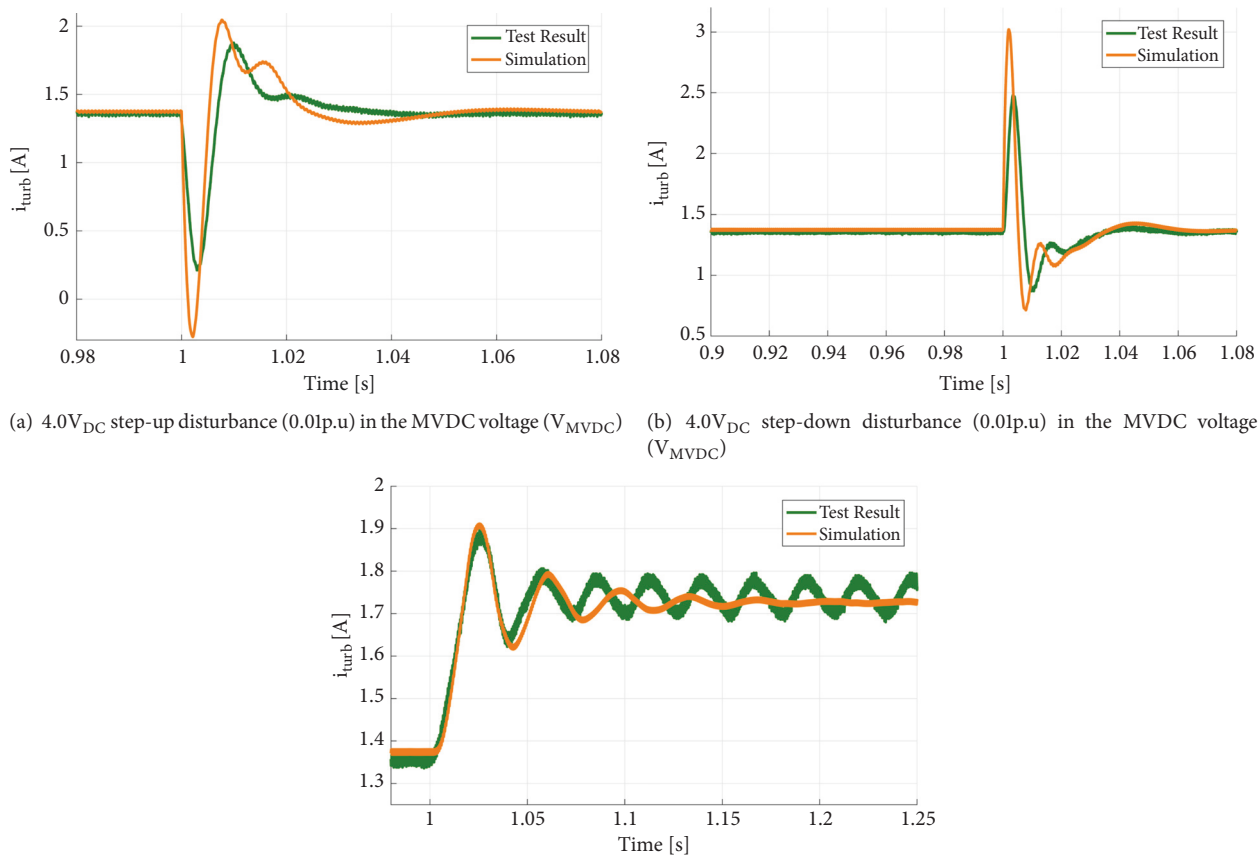

(a) $4.0V_{DC}$ step-up disturbance (0.01p.u) in the MVDC voltage (V_{MVDC})

(b) $4.0V_{DC}$ step-down disturbance (0.01p.u) in the MVDC voltage (V_{MVDC})

(c) Step-up disturbance (0.26p.u) in the power reference signal P_{REF} (equivalent of current reference signal: 1.37A⟶1.73A)

Figure 16: Dynamic response of output current of DC wind turbine converter (i_{turb}) when a step-up/-down disturbance is injected in system at t=1.0 [s].

operating points (different output powers). Integrating the gain scheduling controller with closed-loop structure enables the system to automatically adjust parameters of controller in real time to satisfy different output power requirements without sacrificing the control performance. Finally, Section 8 shows that all the test results give enough supporting arguments to the proposed control design.

Appendix

The objective of the study is to understand the harmonics distribution of offshore DC wind farm and how the DC wind turbines are affected by harmonics from MVDC gird. This section summarizes the derivation of plant model of DC wind turbine based on the discrete time domain modelling approach (discrete time domain modelling approach [10], steps 1-8) which can help the reader to reach the plant model of DC wind turbine (SRC#) and then conduct control deign of DC wind turbine. The following discussion will give a complete derivation process including the corresponding flow chart of the derivation of SRC# plant model given in Figure 4.

Steps 1 -3: Decide the Circuit Topology of DC Turbine Converter, Resonant Tank Waveform, and Equivalent Circuit. Steps 1-3 describe the circuit topology of SRC# (DC wind turbine converter) and mode of operation, which is operated in subresonant CCM as in Figures 2 and 5. The corresponding equivalent circuit for the SRC# in subresonant CCM is given in Figure 6, where the waveform is divided by different time zone (different switching sequence) based on the *discrete time domain modelling* approach proposed by King, R. J. [10]. Those figures (Figures 2, 5, and 6) are used to generate the large signal model of SRC#.

Step 4: Large Signal Model. Based on Figure 6, the objective of derivation of large-signal model is to express the final value of interesting state variables in each switching interval with the initial values. The procedure is only valid when the variation in output voltage $v_o(t)$ (MVDC grid voltage) or input voltage $v_g(t)$ (LVDC voltage) in the event (switching) is relatively smaller than its initial and final values [10]. Equations (A.1) to (A.16) give the derivation of large-signal model of resonant inductor current i_r(t) and resonant capacitor voltage v_{Cr}(t) and their end values at k_{th} event in terms of initial values of k_{th} event.

For $t_{0(k)} \le t \le t_{1(k)}$ (T_1, T_4 ON)

$$v_g = L_r \frac{di_r}{dt} + v_{Cr} + v_o,$$

$$i_r = C_r \frac{dv_{Cr}}{dt} \tag{A.1}$$

where

$$v_g = V_{g,0(k)}, \quad v_o = V_{o,0(k)} \tag{A.2}$$

The resonant inductor current $i_r(t)$ and resonant capacitor voltage $v_{Cr}(t)$ can be obtained by solving (A.1).

$$i_r = \frac{1}{Z_r}\left(V_{g,0(k)} - V_{o,0(k)} - V_{Cr,0(k)}\right)\sin\left(\omega_r t\right) + I_{r,0(k)}\cos\left(\omega_r t\right), \tag{A.3}$$

$$v_{Cr} = V_{g,0(k)} - \left(V_{g,0(k)} - V_{o,0(k)} - V_{Cr,0(k)}\right)\cos\left(\omega_r t\right) + I_{r,0(k)} Z_r \sin\left(\omega_r t\right) - V_{o,0(k)} \tag{A.4}$$

where

$$Z_r = \sqrt{\frac{L_r}{C_r}}, \quad \omega_r = \frac{1}{\sqrt{L_r C_r}} \tag{A.5}$$

At time $t = t_{1(k)}$ the tank current i_r makes a zero crossing, commutating T_1 and T_4 off and turning on D_1 and T_3. Therefore,

$$I_{r,1(k)} = i_r\left(t_{1(k)}\right) = \frac{1}{Z_r}\left(V_{g,0(k)} - V_{o,0(k)} - V_{Cr,0(k)}\right)\sin\left(\omega_r t_{1(k)}\right) + I_{r,0(k)}\cos\left(\omega_r t_{1(k)}\right) = 0 \tag{A.6}$$

where

$$\omega_r t_{1(k)} = \frac{\omega_r}{\omega_s}\beta_K = \omega_{rs}\cdot\beta_K \quad for\ t_{0(k)} = 0 \tag{A.7}$$

$$\tan\left(\omega_{rs}\beta_K\right) = \frac{-I_{r,0(k)} Z_r}{\left(V_{g,0(k)} - V_{o,0(k)} - V_{Cr,0(k)}\right)}, \tag{A.8}$$

$$0 < \left(\omega_{rs}\beta_K\right) \le \pi, \quad t_{1(k)} = \frac{\beta_K}{\omega_s} \tag{A.9}$$

$$V_{Cr,1(k)} = v_{Cr}\left(t_{1(k)}\right) = V_{g,0(k)} - \left(V_{g,0(k)} - V_{o,0(k)} - V_{Cr,0(k)}\right)\cdot\cos\left(\omega_{rs}\beta_K\right) + I_{r,0(k)} Z_r \cdot\sin\left(\omega_{rs}\beta_K\right) - V_{o,0(k)} \tag{A.10}$$

For $t_{1(k)} \le t \le t_{2(k)}$ (D_1, T_3 ON)

$$i_r\left(t'\right) = \frac{-1}{Z_r}\left(V_{o,1(k)} + V_{Cr,1(k)}\right)\sin\left(\omega_r t'\right) \tag{A.11}$$

where

$$t' = t - t_{1(k)}, \tag{A.12}$$

$$v_{Cr}\left(t'\right) = \left(V_{o,1(k)} + V_{Cr,1(k)}\right)\cos\left(\omega_r t'\right) - V_{o,1(k)} \tag{A.13}$$

where

$$I_{r,1(k)} = 0, \quad V_{g,1(k)} = 0, \quad V_{o,1(k)} = -V_{MVDC} = -V_{o,0(k)} \tag{A.14}$$

Eventually, the inductor current $i_r(t)$ and capacitor voltage $v_{Cr}(t)$ at time $t=t_{2(k)}$ can be represented by

$$\begin{aligned} I_{r,2(k)} &= \left[-\sin\left(\omega_{rs}\beta_K\right)\cdot\sin\left(\omega_{rs}\alpha_K\right)\right]\cdot I_{r,0(k)} \\ &+ \left[-\frac{1}{Z_r}\cdot\cos\left(\omega_{rs}\beta_K\right)\cdot\sin\left(\omega_{rs}\alpha_K\right)\right]\cdot V_{Cr,0(k)} \\ &+ \left[\frac{2}{Z_r}\cdot\sin\left(\omega_{rs}\alpha_K\right) + \frac{-1}{Z_r}\cdot\cos\left(\omega_{rs}\beta_K\right)\cdot\sin\left(\omega_{rs}\alpha_K\right)\right]\cdot V_{o,0(k)} + \left[\frac{-1}{Z_r}\cdot\sin\left(\omega_{rs}\alpha_K\right) + \frac{1}{Z_r}\cdot\cos\left(\omega_{rs}\beta_K\right)\cdot\sin\left(\omega_{rs}\alpha_K\right)\right]\cdot V_{g,0(k)}, \end{aligned} \tag{A.15}$$

$$\begin{aligned} V_{Cr,2(k)} &= \left[Z_r\cdot\sin\left(\omega_{rs}\beta_K\right)\cdot\cos\left(\omega_{rs}\alpha_K\right)\right]\cdot I_{r,0(k)} \\ &+ \left[\cos\left(\omega_{rs}\beta_K\right)\cdot\cos\left(\omega_{rs}\alpha_K\right)\right]\cdot V_{Cr,0(k)} + \left[-2\cdot\cos\left(\omega_{rs}\alpha_K\right) + \cos\left(\omega_{rs}\beta_K\right)\cdot\cos\left(\omega_{rs}\alpha_K\right) + 1\right]\cdot V_{o,0(k)} + \left[\cos\left(\omega_{rs}\alpha_K\right) - \cos\left(\omega_{rs}\beta_K\right)\cdot\cos\left(\omega_{rs}\alpha_K\right)\right]\cdot V_{g,0(k)} \end{aligned} \tag{A.16}$$

where

$$\omega_s\cdot\left(t_{2(k)} - t_{1(k)}\right) = \alpha_K \tag{A.17}$$

The large-signal expression of resonant inductor current $i_r(t)$ and resonant capacitor voltage $v_{Cr}(t)$ in $(k+1)_{th}$ event ($t_{0(k+1)} \le t \le t_{1(k+1)}$ and $t_{1(k+1)} \le t \le t_{2(k+1)}$) can be obtained with the same process as derivation of equations, as in (A.1)-(A.16).

Steady-State Solution of Large-Signal Model. Equation (A.18) gives the conditions for calculating steady-state solution (operating points) of discrete state equation.

$$I_{r,2(k)} = -I_{r,0(k)}, \quad V_{Cr,2(k)} = -V_{Cr,0(k)} \tag{A.18}$$

By substituting (A.18) into (A.15) and (A.16), the steady-state solution of $I_{r,0(k)}$ and $V_{Cr,0(k)}$ can be expressed in terms of $V_{o,0(k)}$, $V_{g,0(k)}$, β_k, and α_k:

$$\overline{I}_r = I_{r,0(k)} = f\left(V_{o,0(k)}, V_{g,0(k)}, \beta_K, \alpha_k\right), \tag{A.19}$$

$$\overline{V}_{Cr} = V_{Cr,0(\mathrm{k})} = f\left(V_{o,0(k)}, V_{g,0(k)}, \beta_K, \alpha_k\right) \tag{A.20}$$

where the overbar is used to indicated the steady-state value of interesting state variables.

To simplify the derivation, the output filter of SRC (i.e., L_f and C_f) is neglected due to very slow dynamics in voltage and current compared with the resonant inductor current and resonant capacitor and only the DC component of output current diode rectifier $i_{out,Rec}$ is selected as an output variable i_o. Therefore, during the K_{th} event, the output current equation delivered by the SRC is expressed as

$$\begin{aligned}
i_o &= \frac{1}{\gamma_k}\int_0^{\beta_k} i_{out,\mathrm{Rec}}(\theta_s)\,d\theta_s + \frac{1}{\gamma_k}\int_{\beta_k}^{\gamma_k} i_{out,\mathrm{Rec}}(\theta_s)\,d\theta_s \\
&= \frac{1}{\gamma_k}\cdot\left\{\frac{1}{\omega_{rs}}\sin(\omega_{rs}\beta_k) + \frac{1}{\omega_{rs}}\sin(\omega_{rs}\beta_K)\right. \\
&\quad \left.\cdot\left[1-\cos(\omega_{rs}\alpha_k)\right]\right\}\cdot I_{r,0(k)} + \frac{1}{\gamma_k} \\
&\quad \cdot\left\{-\frac{1}{\omega_{rs}}\frac{1}{Z_r}\left[1-\cos(\omega_{rs}\beta_k)\right]\right. \\
&\quad \left.+\frac{1}{\omega_{rs}}\frac{1}{Z_r}\cos(\omega_{rs}\beta_K)\cdot\left[1-\cos(\omega_{rs}\alpha_k)\right]\right\} \\
&\quad \cdot V_{Cr,0(\mathrm{k})} + \frac{1}{\gamma_k}\cdot\left\{-\frac{1}{\omega_{rs}}\frac{1}{Z_r}\left[1-\cos(\omega_{rs}\beta_k)\right]\right. \\
&\quad \left.+\frac{1}{\omega_{rs}}\frac{1}{Z_r}\left(\cos(\omega_{rs}\beta_K)-2\right)\cdot\left[1-\cos(\omega_{rs}\alpha_k)\right]\right\} \\
&\quad \cdot V_{o,0(k)} + \frac{1}{\gamma_k}\cdot\left\{\frac{1}{\omega_{rs}}\frac{1}{Z_r}\left[1-\cos(\omega_{rs}\beta_k)\right]\right. \\
&\quad \left.+\frac{1}{\omega_{rs}}\frac{1}{Z_r}\left(1-\cos(\omega_{rs}\beta_K)\right)\cdot\left[1-\cos(\omega_{rs}\alpha_k)\right]\right\} \\
&\quad \cdot V_{g,0(k)}
\end{aligned} \tag{A.21}$$

where

$$\begin{aligned}
\theta_s &= \omega_s t, \\
\alpha_k &= \gamma_k - \beta_k
\end{aligned} \tag{A.22}$$

and $I_{r,0(k)}$ is the initial value of Inductor current, $V_{Cr,0(k)}$ is the initial value of capacitor voltage, $V_{o,0(k)}$ is the initial value of rectifier output voltage, and $V_{g,0(k)}$ is then initial value of input voltage of SRC#. Z_r ($=\sqrt{(L_r/C_r)}$) is characteristic impedance defined by parameter of resonant tanks, α_k ($=\gamma_k$-β_k) is the transistor and diode conduction angle during the switching interval (event k), and θ_s ($=\omega_s\ t$) is represented by the switching frequency of converter.

The steady-state solution of discrete state equation for output variable i_o is obtained by substituting steady-state condition into (A.21) as

$$\begin{aligned}
&\overline{I}_o \\
&= i_o\big|_{(\beta_k=\overline{\beta},\alpha_k=\overline{\alpha},\gamma_k=\overline{\gamma},I_{r,0(\mathrm{k})}=\overline{I}_r,V_{Cr,0(\mathrm{k})}=\overline{V}_{cr},V_{o,0(\mathrm{k})}=\overline{V}_o,V_{g,0(\mathrm{k})}=\overline{V}_g)}
\end{aligned} \tag{A.23}$$

Step 5: Define State Variable. Since the discrete large-signal state equations in (A.15), (A.16), and (A.21) have a high nonlinearity, control design technique based on the linear control theory cannot directly be applied. To obtain a linear state-space model, therefore, the linearization of large-signal equation is necessary. Equation (A.24) gives the definitions of interesting state variables in both the k_{th} switching event ($\mathrm{t}_{0(\mathrm{k})} \le \mathrm{t} \le \mathrm{t}_{2(\mathrm{k})}$) and the $(k+1)_{th}$ switching event ($\mathrm{t}_{2(\mathrm{k})} \le \mathrm{t} \le \mathrm{t}_{2(\mathrm{k}+1)}$). Finally, the equations of approximation of derivative in (A.24) and (A.25) are used to convert the discrete state-equation (large-signal model) into continuous time [10].

$$\begin{aligned}
x_{1(k)} &= I_{r,0(k)}, \\
x_{2(k)} &= V_{Cr,0(\mathrm{k})} \\
I_{r,2(k)} &= -x_{1(k+1)}, \\
V_{Cr,2(k)} &= -x_{2(k+1)},
\end{aligned} \tag{A.24}$$

$$\dot{x}_i(\mathrm{t}_k) = \frac{x_{i,(\mathrm{k}+1)} - x_{i,(k)}}{t_{0(\mathrm{k}+1)} - t_{0(k)}} = \frac{\omega_s}{\gamma_k}\left(x_{i,(\mathrm{k}+1)} - x_{i,(k)}\right) \tag{A.25}$$

where

$$\gamma_k = \omega_s\left(t_{2(\mathrm{k})} - t_{0(\mathrm{k})}\right) = \omega_s\left(t_{0(\mathrm{k}+1)} - t_{0(k)}\right) \tag{A.26}$$

By replacing the state variables in (A.15) and (A.16) with the defined state variables in (A.24) and applying the approximation of (A.25) for derivative, the nonlinear state-space model is given by

$$\begin{aligned}
\dot{x}_{1(\mathrm{k})} &= \frac{\omega_s}{\gamma_k}\cdot\left[\sin(\omega_{rs}\beta_K)\cdot\sin(\omega_{rs}\alpha_K) - 1\right]\cdot x_{1(k)} \\
&\quad + \frac{\omega_s}{\gamma_k}\cdot\left[\frac{1}{Z_r}\cdot\cos(\omega_{rs}\beta_K)\cdot\sin(\omega_{rs}\alpha_K)\right]\cdot x_{2(k)} \\
&\quad + \frac{\omega_s}{\gamma_k}\cdot\left[\frac{-2}{Z_r}\cdot\sin(\omega_{rs}\alpha_K) + \frac{1}{Z_r}\cdot\cos(\omega_{rs}\beta_K)\right. \\
&\quad \left.\cdot\sin(\omega_{rs}\alpha_K)\right]\cdot V_{o,0(k)} + \frac{\omega_s}{\gamma_k}\cdot\left[\frac{1}{Z_r}\cdot\sin(\omega_{rs}\alpha_K)\right. \\
&\quad \left.+\frac{-1}{Z_r}\cdot\cos(\omega_{rs}\beta_K)\cdot\sin(\omega_{rs}\alpha_K)\right]\cdot V_{g,0(k)} \\
&= f_1\left\{x_{1(k)}, x_{2(k)}, V_{o,0(k)}, V_{g,0(k)}, \alpha_k\right\} \\
&= f_1\left\{x_1, x_2, v_o, v_g, \alpha\right\} = \frac{\omega_s}{\gamma_k} \\
&\quad \cdot f_1^*\left\{x_1, x_2, v_o, v_g, \alpha\right\}
\end{aligned} \tag{A.27}$$

$$\begin{aligned}\dot{x}_{2(k)} &= \frac{\omega_s}{\gamma_k}\cdot\left[-Z_r\cdot\sin\left(\omega_{rs}\beta_K\right)\cdot\cos\left(\omega_{rs}\alpha_K\right)\right]\\ &\cdot x_{1(k)}+\frac{\omega_s}{\gamma_k}\cdot\left[-\cos\left(\omega_{rs}\beta_K\right)\cdot\cos\left(\omega_{rs}\alpha_K\right)-1\right]\\ &\cdot x_{2(k)}+\frac{\omega_s}{\gamma_k}\cdot\left[2\cdot\cos\left(\omega_{rs}\alpha_K\right)-\cos\left(\omega_{rs}\beta_K\right)\right.\\ &\left.\cdot\cos\left(\omega_{rs}\alpha_K\right)-1\right]\cdot V_{o,0(k)}+\frac{\omega_s}{\gamma_k}\cdot\left[-\cos\left(\omega_{rs}\alpha_K\right)\right.\\ &\left.+\cos\left(\omega_{rs}\beta_K\right)\cdot\cos\left(\omega_{rs}\alpha_K\right)\right]\cdot V_{g,0(k)}\\ &= f_2\left\{x_{1(k)},x_{2(k)},V_{o,0(k)},V_{g,0(k)},\alpha_k\right\}\\ &= f_2\left\{x_1,x_2,v_o,v_g,\alpha\right\}=\frac{\omega_s}{\gamma_k}\\ &\cdot f_2^*\left\{x_1,x_2,v_o,v_g,\alpha\right\}\end{aligned}\tag{A.28}$$

where the output equation is defined as

$$\begin{aligned}i_o &= f_{out}\left\{x_{1(k)},x_{2(k)},V_{o,0(k)},V_{g,0(k)},\alpha_k\right\}\\ &= f_{out}\left\{x_1,x_2,v_o,v_g,\alpha\right\}\\ &= \frac{1}{\gamma_k}\cdot f_{out}^*\left\{x_1,x_2,v_o,v_g,\alpha\right\}\end{aligned}\tag{A.29}$$

Step 6: Linearization and Small-Signal Model. Consider that all the interesting state variables in pervious steps are in the steady-state (near the certain operating point, *OP*) with a small perturbation; therefore, the nonlinear state equations can be formalized with *Taylor Series Expansion* in terms of the operating point (*OP*) and the perturbations:

(i) Resonant inductor current:

$$\begin{aligned}[\dot{\overline{x}_1+\tilde{x}_1}] &= f_1\left\{\overline{x}_1+\tilde{x}_1,\overline{x}_2+\tilde{x}_2,\overline{V}_o+\tilde{V}_o,\overline{V}_g\right.\\ &\left.+\tilde{V}_g,\overline{\alpha}+\tilde{\alpha}\right\}=\frac{\omega_s}{\gamma_k}\cdot f_1^*\left\{\overline{x}_1+\tilde{x}_1,\overline{x}_2+\tilde{x}_2,\overline{V}_o\right.\\ &\left.+\tilde{V}_o,\overline{V}_g+\tilde{V}_g,\overline{\alpha}+\tilde{\alpha}\right\}\end{aligned}\tag{A.30}$$

where

$$\begin{aligned}x_1 &= \overline{x}_1+\tilde{x}_1,\\ x_2 &= \overline{x}_2+\tilde{x}_2,\\ v_g &= \overline{V}_g+\tilde{V}_g,\\ v_o &= \overline{V}_o+\tilde{V}_o,\\ \alpha &= \overline{\alpha}+\tilde{\alpha}\end{aligned}\tag{A.31}$$

and then

$$\begin{aligned}[\dot{\overline{x}_1+\tilde{x}_1}] &= f_1\left\{\overline{x}_1,\overline{x}_2,\overline{V}_o,\overline{V}_g,\overline{\alpha}\right\}+\left.\frac{\partial f_1}{\partial x_1}\right|_{OP}\tilde{x}_1\\ &+\left.\frac{\partial f_1}{\partial x_2}\right|_{OP}\tilde{x}_2+\left.\frac{\partial f_1}{\partial v_g}\right|_{OP}\tilde{V}_g\\ &+\left.\frac{\partial f_1}{\partial v_o}\right|_{OP}\tilde{V}_o+\left.\frac{\partial f_1}{\partial \alpha}\right|_{OP}\tilde{\alpha}\\ &+\frac{1}{2!}\left.\frac{\partial^2 f_1}{\partial x_1^2}\right|_{OP}\tilde{x}_1^{\,2}+\cdots\end{aligned}\tag{A.32}$$

where the subscript *OP* indicates the steady-state point, where the derivatives are evaluated at that point.

$$\begin{aligned}OP &= \overline{I}_r,\overline{V}_{Cr},\overline{V}_o,\overline{V}_g,\overline{\alpha},\\ f_1\left\{\overline{x}_1,\overline{x}_2,\overline{V}_o,\overline{V}_g,\overline{\alpha}\right\} &= \dot{\overline{I}}_r=0\end{aligned}\tag{A.33}$$

(ii) Resonant capacitor voltage:

$$\begin{aligned}[\dot{\overline{x}_2+\tilde{x}_2}] &= f_2\left\{\overline{x}_1+\tilde{x}_1,\overline{x}_2+\tilde{x}_2,\overline{V}_o+\tilde{V}_o,\overline{V}_g\right.\\ &\left.+\tilde{V}_g,\overline{\alpha}+\tilde{\alpha}\right\}=\frac{\omega_s}{\gamma_k}\cdot f_2^*\left\{\overline{x}_1+\tilde{x}_1,\overline{x}_2+\tilde{x}_2,\overline{V}_o\right.\\ &\left.+\tilde{V}_o,\overline{V}_g+\tilde{V}_g,\overline{\alpha}+\tilde{\alpha}\right\}\end{aligned}\tag{A.34}$$

where

$$\begin{aligned}x_1 &= \overline{x}_1+\tilde{x}_1,\\ x_2 &= \overline{x}_2+\tilde{x}_2,\\ v_g &= \overline{V}_g+\tilde{V}_g,\\ v_o &= \overline{V}_o+\tilde{V}_o,\\ \alpha &= \overline{\alpha}+\tilde{\alpha}\end{aligned}\tag{A.35}$$

and then

$$\begin{aligned}[\dot{\overline{x}_2+\tilde{x}_2}] &= f_2\left\{\overline{x}_1,\overline{x}_2,\overline{V}_o,\overline{V}_g,\overline{\alpha}\right\}+\left.\frac{\partial f_2}{\partial x_1}\right|_{OP}\tilde{x}_1\\ &+\left.\frac{\partial f_2}{\partial x_2}\right|_{OP}\tilde{x}_2+\left.\frac{\partial f_2}{\partial v_g}\right|_{OP}\tilde{V}_g\\ &+\left.\frac{\partial f_2}{\partial v_o}\right|_{OP}\tilde{V}_o+\left.\frac{\partial f_2}{\partial \alpha}\right|_{OP}\tilde{\alpha}\\ &+\frac{1}{2!}\left.\frac{\partial^2 f_2}{\partial x_1^2}\right|_{OP}\tilde{x}_1^{\,2}+\cdots\end{aligned}\tag{A.36}$$

where

$$f_2\left\{\overline{x}_1,\overline{x}_2,\overline{V}_o,\overline{V}_g,\overline{\alpha}\right\}=\dot{\overline{V}}_{Cr}=0\tag{A.37}$$

(iii) Output current equation:

$$\begin{aligned}\overline{I}_o+\tilde{I}_o &= f_{out}\left\{\overline{x}_1+\tilde{x}_1,\overline{x}_2+\tilde{x}_2,\overline{V}_o+\tilde{V}_o,\overline{V}_g\right.\\ &\left.+\tilde{V}_g,\overline{\alpha}+\tilde{\alpha}\right\}=\frac{1}{(\overline{\gamma}+\tilde{\gamma})}\cdot f_{out}^*\left\{\overline{x}_1+\tilde{x}_1,\overline{x}_2\right.\\ &\left.+\tilde{x}_2,\overline{V}_o+\tilde{V}_o,\overline{V}_g+\tilde{V}_g,\overline{\alpha}+\tilde{\alpha}\right\}\end{aligned}\tag{A.38}$$

where

$$\begin{aligned} x_1 &= \overline{x}_1 + \widetilde{x}_1, \\ x_2 &= \overline{x}_2 + \widetilde{x}_2, \\ v_g &= \overline{V}_g + \widetilde{V}_g, \\ v_o &= \overline{V}_o + \widetilde{V}_o, \\ \alpha &= \overline{\alpha} + \widetilde{\alpha}, \\ \widetilde{\gamma} &= \widetilde{\alpha} + \widetilde{\beta} \end{aligned} \tag{A.39}$$

and then

$$\begin{aligned} \overline{I}_o + \widetilde{I}_o &= f_{out}\left\{\overline{x}_1, \overline{x}_2, \overline{V}_o, \overline{V}_g, \overline{\alpha}\right\} + \left.\frac{\partial f_{out}}{\partial x_1}\right|_{OP} \widetilde{x}_1 \\ &+ \left.\frac{\partial f_{out}}{\partial x_2}\right|_{OP} \widetilde{x}_2 + \left.\frac{\partial f_{out}}{\partial v_g}\right|_{OP} \widetilde{V}_g + \left.\frac{\partial f_{out}}{\partial v_o}\right|_{OP} \widetilde{V}_o \\ &+ \left.\frac{\partial f_{out}}{\partial \alpha}\right|_{OP} \widetilde{\alpha} + \frac{1}{2!} \left.\frac{\partial^2 f_{out}}{\partial x_1{}^2}\right|_{OP} \widetilde{x}_1{}^2 + \cdots = \frac{1}{\overline{\gamma}} \cdot \left\{1 \right. \\ &\left. - \left(\frac{\widetilde{\gamma}}{\overline{\gamma}}\right) + \left(\frac{\widetilde{\gamma}}{\overline{\gamma}}\right)^2 - \ldots + \ldots \right\} \\ &\cdot \left\{ f^*_{out}\left\{\overline{x}_1, \overline{x}_2, \overline{V}_o, \overline{V}_g, \overline{\alpha}\right\} + \left.\frac{\partial f^*_{out}}{\partial x_1}\right|_{OP} \widetilde{x}_1 \right. \\ &+ \left.\frac{\partial f^*_{out}}{\partial x_2}\right|_{OP} \widetilde{x}_2 + \left.\frac{\partial f^*_{out}}{\partial v_g}\right|_{OP} \widetilde{V}_g + \left.\frac{\partial f_{out}}{\partial v_o}\right|_{OP} \widetilde{V}_o \\ &+ \left.\frac{\partial f^*_{out}}{\partial \alpha}\right|_{OP} \widetilde{\alpha} + \frac{1}{2!} \left.\frac{\partial^2 f^*_{out}}{\partial x_1{}^2}\right|_{OP} \widetilde{x}_1{}^2 + \cdots \Bigg\} \end{aligned} \tag{A.40}$$

where

$$\begin{aligned} \overline{I}_o &= f_{out}\left\{\overline{x}_1, \overline{x}_2, \overline{V}_o, \overline{V}_g, \overline{\alpha}\right\} \\ \widetilde{I}_o &= \frac{1}{\overline{\gamma}} \cdot \left\{ \left[\left.\frac{\partial f^*_{out}}{\partial x_1}\right|_{OP} - \overline{I}_o \cdot \left.\frac{\partial \beta}{\partial x_1}\right|_{OP} \right] \cdot \widetilde{x}_1 \right. \\ &+ \left[\left.\frac{\partial f^*_{out}}{\partial x_2}\right|_{OP} - \overline{I}_o \cdot \left.\frac{\partial \beta}{\partial x_2}\right|_{OP} \right] \cdot \widetilde{x}_2 \\ &+ \left[\left.\frac{\partial f^*_{out}}{\partial v_g}\right|_{OP} - \overline{I}_o \cdot \left.\frac{\partial \beta}{\partial v_g}\right|_{OP} \right] \cdot \widetilde{V}_g \\ &+ \left[\left.\frac{\partial f^*_{out}}{\partial v_o}\right|_{OP} - \overline{I}_o \cdot \left.\frac{\partial \beta}{\partial v_o}\right|_{OP} \right] \cdot \widetilde{V}_o \\ &+ \left. \left[\left.\frac{\partial f^*_{out}}{\partial \alpha}\right|_{OP} - \overline{I}_o \right] \cdot \widetilde{\alpha} \right\} \end{aligned} \tag{A.41}$$

Neglect the higher-order terms of perturbation signals and retain only the linear terms in *Taylor Series Expansion* to obtain the linearized equations for (A.32), (A.36), and (A.40).

Step 7: State-Space Model. Equation (A.42) gives a linearized state-space model of SRC in subresonant mode from (A.32), (A.36), and (A.40) and the transfer functions between input state variables and the defined states are summarized in (A.50) and (A.52).

$$\begin{aligned} \begin{bmatrix} \dot{\widetilde{x}}_1 \\ \dot{\widetilde{x}}_2 \end{bmatrix} &= \begin{bmatrix} \left.\frac{\partial f_1}{\partial x_1}\right|_{OP} & \left.\frac{\partial f_1}{\partial x_2}\right|_{OP} \\ \left.\frac{\partial f_2}{\partial x_1}\right|_{OP} & \left.\frac{\partial f_2}{\partial x_2}\right|_{OP} \end{bmatrix} \begin{bmatrix} \widetilde{x}_1 \\ \widetilde{x}_2 \end{bmatrix} + \begin{bmatrix} \left.\frac{\partial f_1}{\partial \alpha}\right|_{OP} & \left.\frac{\partial f_1}{\partial v_g}\right|_{OP} & \left.\frac{\partial f_1}{\partial v_o}\right|_{OP} \\ \left.\frac{\partial f_2}{\partial \alpha}\right|_{OP} & \left.\frac{\partial f_2}{\partial v_g}\right|_{OP} & \left.\frac{\partial f_2}{\partial v_o}\right|_{OP} \end{bmatrix} \begin{bmatrix} \widetilde{\alpha} \\ \widetilde{V}_g \\ \widetilde{V}_o \end{bmatrix} \\ \widetilde{I}_o &= \left[\frac{1}{\overline{\gamma}} \cdot \left[\left.\frac{\partial f^*_{out}}{\partial x_1}\right|_{OP} - \overline{I}_o \cdot \left.\frac{\partial \beta}{\partial x_1}\right|_{OP} \right] \; \frac{1}{\overline{\gamma}} \cdot \left[\left.\frac{\partial f^*_{out}}{\partial x_2}\right|_{OP} - \overline{I}_o \cdot \left.\frac{\partial \beta}{\partial x_2}\right|_{OP} \right] \right] \begin{bmatrix} \widetilde{x}_1 \\ \widetilde{x}_2 \end{bmatrix} \\ &+ \left[\frac{1}{\overline{\gamma}} \cdot \left[\left.\frac{\partial f^*_{out}}{\partial \alpha}\right|_{OP} - \overline{I}_o \right] \; \frac{1}{\overline{\gamma}} \cdot \left[\left.\frac{\partial f^*_{out}}{\partial v_g}\right|_{OP} - \overline{I}_o \cdot \left.\frac{\partial \beta}{\partial v_g}\right|_{OP} \right] \; \frac{1}{\overline{\gamma}} \cdot \left[\left.\frac{\partial f_{out}}{\partial v_o}\right|_{OP} - \overline{I}_o \cdot \left.\frac{\partial \beta}{\partial v_o}\right|_{OP} \right] \right] \begin{bmatrix} \widetilde{\alpha} \\ \widetilde{V}_g \\ \widetilde{V}_o \end{bmatrix} \end{aligned} \tag{A.42}$$

For derivative of equations f_1 and f_2,

$$\frac{\partial f_i}{\partial x_j} = \left(\frac{\partial}{\partial x_j} \frac{\omega_s}{\gamma}\right) \cdot \left. f^*_i \right|_{OP} + \frac{\omega_s}{\gamma} \left.\frac{\partial f^*_i}{\partial x_j}\right|_{OP} \tag{A.43}$$

where

$$\gamma = \alpha + \beta \quad \textit{for } i = 1, 2, \;\; j = 1, 2 \tag{A.44}$$

With the steady-state operating conditions,

$$\begin{aligned} \left.\frac{\omega_s}{\gamma}\right|_{OP} &\neq 0, \\ \left. f^*_i \right|_{OP} &= 0 \end{aligned} \tag{A.45}$$

Therefore,

$$\frac{\partial f_i}{\partial x_j} = \frac{\omega_s}{\gamma} \left.\frac{\partial f_i^*}{\partial x_j}\right|_{OP} \tag{A.46}$$

The same approach as the derivative of f_1 and f_2 with respect to input states x_1 and x_2 can be used to evaluate the derivative of $f^*{}_{out}$ and the derivative of f_1 and f_2 with respect to input states α, v_g, and v_o.

According to the derivation of large signal model in (A.8), the angle β and its steady-state solution can be expressed by

$$\tan(\omega_{rs}\beta) = \frac{-x_1 Z_r}{(v_g - v_o - x_2)} = \tan(\omega_{rs}\beta - \pi), \tag{A.47}$$

$$\begin{aligned} \beta|_{OP} &= \frac{\pi}{\omega_{rs}} + \frac{1}{\omega_{rs}} \\ &\quad \cdot \tan^{-1}\left[\frac{-\overline{I}_r Z_r}{(\overline{V}_g - \overline{V}_o - \overline{V}_{Cr})}\right] \end{aligned} \tag{A.48}$$

The derivatives of β with respect to input states x_1, x_2, v_g, and v_o at the given operating points are

$$\begin{aligned} \left.\frac{\partial\beta}{\partial x_1}\right|_{OP} &= \left.\left[\frac{1}{\omega_{rs}} \cdot \frac{-Z_r \cdot (v_g - v_o - x_2)}{(v_g - v_o - x_2)^2 + (x_1 Z_r)^2}\right]\right|_{OP} \\ &= \frac{1}{\omega_{rs}} \cdot \frac{-Z_r \cdot (\overline{V}_g - \overline{V}_o - \overline{V}_{Cr})}{(\overline{V}_g - \overline{V}_o - \overline{V}_{Cr})^2 + (\overline{I}_r Z_r)^2} \\ \left.\frac{\partial\beta}{\partial x_2}\right|_{OP} &= \left.\left[\frac{1}{\omega_{rs}} \cdot \frac{-x_1 Z_r}{(v_g - v_o - x_2)^2 + (x_1 Z_r)^2}\right]\right|_{OP} \\ &= \frac{1}{\omega_{rs}} \cdot \frac{-\overline{I}_r Z_r}{(\overline{V}_g - \overline{V}_o - \overline{V}_{Cr})^2 + (\overline{I}_r Z_r)^2} \\ \left.\frac{\partial\beta}{\partial v_0}\right|_{OP} &= \left.\left[\frac{1}{\omega_{rs}} \cdot \frac{-x_1 Z_r}{(v_g - v_o - x_2)^2 + (x_1 Z_r)^2}\right]\right|_{OP} \\ &= \frac{1}{\omega_{rs}} \cdot \frac{-\overline{I}_r Z_r}{(\overline{V}_g - \overline{V}_o - \overline{V}_{Cr})^2 + (\overline{I}_r Z_r)^2} \\ \left.\frac{\partial\beta}{\partial v_g}\right|_{OP} &= \left.\left[\frac{1}{\omega_{rs}} \cdot \frac{x_1 Z_r}{(v_g - v_o - x_2)^2 + (x_1 Z_r)^2}\right]\right|_{OP} \\ &= \frac{1}{\omega_{rs}} \cdot \frac{\overline{I}_r Z_r}{(\overline{V}_g - \overline{V}_o - \overline{V}_{Cr})^2 + (\overline{I}_r Z_r)^2} \end{aligned} \tag{A.49}$$

where ω_{rs} $(=\omega_r/\omega_s)$ is defined as the ratio between the natural frequency (ω_r) of resonant tank and the switching frequency of converter (ω_s).

Step 8: Transfer Function. The transfer functions between the converter output current (output rectifier current) and input state variables can be obtained with (A.42):

$$\widetilde{I}_o(s) = [g_1(s) \quad g_2(s) \quad g_3(s)] \begin{bmatrix} \widetilde{\alpha} \\ \widetilde{V}_g \\ \widetilde{V}_o \end{bmatrix} \tag{A.50}$$

where

$$\begin{aligned} g_1(s) &= \left.\frac{\widetilde{I}_o(s)}{\widetilde{\alpha}(s)}\right|_{\widetilde{V}_g(s)=0, \widetilde{V}_0(s)=0}, \\ g_2(s) &= \left.\frac{\widetilde{I}_o(s)}{\widetilde{V}_g(s)}\right|_{\widetilde{\alpha}(s)=0, \widetilde{V}_0(s)=0}, \\ g_3(s) &= \left.\frac{\widetilde{I}_o(s)}{\widetilde{V}_0(s)}\right|_{\widetilde{\alpha}(s)=0, \widetilde{V}_g(s)=0}, \\ \widetilde{f}_s &= \widetilde{\alpha}(s) \cdot \frac{f_r}{-\pi} \end{aligned} \tag{A.51}$$

and transfer functions between defined internal state variables and input state are

$$\begin{aligned} \widetilde{X} &= \begin{bmatrix} \widetilde{I}_r \\ \widetilde{v}_{cr} \end{bmatrix} = \begin{bmatrix} \widetilde{x}_1 \\ \widetilde{x}_2 \end{bmatrix} \\ &= \begin{bmatrix} g_{xu,11} & g_{xu,12} & g_{xu,13} \\ g_{xu,21} & g_{xu,22} & g_{xu,23} \end{bmatrix} \begin{bmatrix} \widetilde{\alpha} \\ \widetilde{V}_g \\ \widetilde{V}_o \end{bmatrix} \end{aligned} \tag{A.52}$$

where

$$\begin{aligned} g_{xu,11} &= \left.\frac{\widetilde{I}_r}{\widetilde{\alpha}}\right|_{\widetilde{V}_g(s)=0, \widetilde{V}_0(s)=0}, \\ g_{xu,12} &= \left.\frac{\widetilde{I}_r}{\widetilde{V}_g}\right|_{\widetilde{\alpha}(s)=0, \widetilde{V}_0(s)=0}, \\ g_{xu,13} &= \left.\frac{\widetilde{I}_r}{\widetilde{V}_o}\right|_{\widetilde{\alpha}(s)=0, \widetilde{V}_g(s)=0} \\ g_{xu,21} &= \left.\frac{\widetilde{v}_{cr}}{\widetilde{\alpha}}\right|_{\widetilde{V}_g(s)=0, \widetilde{V}_0(s)=0}, \\ g_{xu,22} &= \left.\frac{\widetilde{v}_{cr}}{\widetilde{V}_g}\right|_{\widetilde{\alpha}(s)=0, \widetilde{V}_0(s)=0}, \\ g_{xu,23} &= \left.\frac{\widetilde{v}_{cr}}{\widetilde{V}_o}\right|_{\widetilde{\alpha}(s)=0, \widetilde{V}_g(s)=0} \end{aligned} \tag{A.53}$$

The derivation of the linearized state-space model and the expression of elements in [A], [B], [C], and [D] matrix are given in (A.42). The transfer functions, $g_1(s)$, $g_2(s)$, and $g_3(s)$, in (A.50) can be obtained by the formula of $C(sI\text{-}A)^{-1}B + D$.

Nomenclature

L_r: Inductor in resonant tank
C_r: Capacitor in resonant tank
i_r: Resonant inductor current
v_{Cr}: Resonant capacitor voltage
v_g: Input voltage of resonant tank referred to as secondary side of medium-frequency transformer
v_o: Output voltage of resonant tank
V_{LVDC}: Low voltage DC
V_{MVDC}: Medium voltage DC
$i_{out,\mathrm{Rec}}$: Output current of diode rectifier
i_{turb}: Output current of DC wind turbine converter
L_f: Inductor in output filter
C_f: Capacitor in output filter
f_s: Switching frequency of series resonant converter defined by $f_s = \omega_s/2\pi$
ω_r: Natural resonant frequency of tank defined by $\omega_r = 1/\sqrt{L_r C_r}$
α_k: Transistor and diode conduction angle during event k
β_k: Transistor conduction angle during event k
γ_k: Total duration of event ($\gamma_k = \alpha_k + \beta_k$).

Data Availability

The authors of the manuscript declare that the data used to support the findings of this study are included within the article.

Conflicts of Interest

The authors declare that they have no conflicts of interest.

References

[1] C. Yu-Hsing et al., "Studies for Characterisation of Electrical Properties of DC Collection System in Offshore Wind Farms," in *Proceedings of the of Cigré General Session 2016*, 2016, article no. B4-301.

[2] V. Vorperian and S. Cuk, "A complete DC analysis of the series resonant converter," in *Proceedings of the 13th Annual IEEE Power Electronics Specialists Conference, (PESC '82)*, pp. 85–100, 1982.

[3] A. F. Witulski and R. W. Erickson, "Steady-State Analysis of the Series Resonant Converter," *IEEE Transactions on Aerospace and Electronic Systems*, vol. 21, no. 6, pp. 791–799, 1985.

[4] R. U. Lenke, J. Hu, and R. W. De Doncker, "Unified steady-state description of phase-shift-controlled ZVS-operated series-resonant and non-resonant single-active-bridge converters," in *Proceedings of the 2009 IEEE Energy Conversion Congress and Exposition, ECCE 2009*, pp. 796–803, IEEE, 2009.

[5] G. Ortiz, H. Uemura, D. Bortis, J. W. Kolar, and O. Apeldoorn, "Modeling of soft-switching losses of IGBTs in high-power high-efficiency dual-active-bridge DC/DC converters," *IEEE Transactions on Electron Devices*, vol. 60, no. 2, pp. 587–597, 2013.

[6] C. Dincan, P. Kjaer, Y. Chen, S. Munk-Nielsen, and C. L. Bak, "Analysis of a High-Power, Resonant DC–DC Converter for DC Wind Turbines," *IEEE Transactions on Power Electronics*, vol. 33, no. 9, pp. 7438–7454, 2017.

[7] R. J. King and T. A. Stuart, "Inherent Overload Protection for the Series Resonant Converter," *IEEE Transactions on Aerospace and Electronic Systems*, vol. 19, no. 6, pp. 820–830, 1983.

[8] H. Wang, T. Saha, and R. Zane, "Control of series connected resonant converter modules in constant current dc distribution power systems," in *Proceedings of the 17th IEEE Workshop on Control and Modeling for Power Electronics, (COMPEL '6)*, pp. 1–7, 2016.

[9] C. Dincan, P. Kjaer, Y. Chen, S. Munk-Nielsen, and C. L. Bak, "A High-Power, Medium-Voltage, Series-Resonant Converter for DC Wind Turbines," *IEEE Transactions on Power Electronics*, 2017.

[10] R. J. King and T. A. Stuart, "Small-Signal Model for the Series Resonant Converter," *IEEE Transactions on Aerospace and Electronic Systems*, vol. 21, no. 3, pp. 301–319, 1985.

[11] R. W. Erickson and D. Maksimovic, *Fundamentals of Power Electronics*, Springer Science & Business Media, 2007.